PHYSICAL REVIEW B **82**, 134514 (2010)

Structural trends from a consistent set of single-crystal data of *R*FeAsO (*R*=La, Ce, Pr, Nd, Sm, Gd, and Tb)

F. Nitsche,[1] A. Jesche,[2] E. Hieckmann,[3] Th. Doert,[1] and M. Ruck[1,2]
[1]*Department of Chemistry and Food Chemistry, Technische Universität Dresden, D-01062 Dresden, Germany*
[2]*Max Planck Institute for Chemical Physics of Solids, D-01187 Dresden, Germany*
[3]*Institute of Applied Physics, Technische Universität Dresden, D-01062 Dresden, Germany*
(Received 4 August 2010; revised manuscript received 14 September 2010; published 11 October 2010)

A crystal-growth technique for single crystals of *R*FeAsO (*R*=La, Ce, Pr, Nd, Sm, Gd, and Tb) using NaI/KI as flux is presented. Crystals with a size up to 300 μm were isolated for single-crystal x-ray diffraction measurements. Lattice parameters were determined by LeBail fits of x-ray powder data against LaB_6 standard. A consistent set of structural data is obtained and interpreted in a hard-sphere model. Effective radii for the rare-earth metal atoms in *R*FeAsO are deduced. The relation of the intraplane and interplane distances of the arsenic atoms is identified as limiter of the phase formation, and its influence on T_c is discussed.

DOI: 10.1103/PhysRevB.82.134514 PACS number(s): 74.70.Xa, 61.66.Fn, 74.62.Bf, 81.10.Dn

I. INTRODUCTION

The discovery of superconductivity in the system LaFePO(F) by Kamihara *et al.*[1] and the subsequent examination of various compounds with a square iron-net substructure such as *R*FeAsO (*R*-1111 with *R*=rare-earth metal), AFe_2As_2 (*A*-122 with *A*=Ca, Sr, Ba, and Eu), *B*FeAs (*B*-111 with *B*=Li, Na, and K), and Fe*Ch* (11 with $Ch=Se_{1-x}Te_x$) revealed a large set of structures and options of doping to study superconductivity.

In the *R*FeAsO compounds, which crystallize in the ZrCuSiAs structure type (Fig. 1), superconductivity can be achieved by electron[2] and hole[3] doping as well as by applying pressure.[4] The underdoped compounds show a tetragonal to orthorhombic transition upon cooling followed by an antiferromagnetic ordering.

The impact of the rare-earth metal atom substitution on the maximal transition temperature ($T_{c,max}$) achievable by doping is shown in Fig. 2. The optimal starting point for electron doping thus seems to be SmFeAsO with the highest achievable T_c for $RFeAsO_{1-\delta}$. The influence of the size of the rare-earth metal atom on the structure of *R*FeAsO and thereby on superconductivity is essential for the understanding of the mechanism of superconductivity as shown by Kuroki *et al.*,[8] who discussed the height of the arsenic atom above the iron atom layer (h_{As}) as a main influence parameter on superconductivity in *R*FeAsO.

Precise information on the evolution of the structures with respect to rare-earth metal substitution and oxygen deficiency concentration is therefore important. Structural information is often obtained by the Rietveld refinement of powder x-ray diffraction data. While this method yields high quality cell parameters, structural refinement of single-crystal x-ray diffraction data offers a more accurate determination of the structural parameters including displacement parameters.

Single crystals of PrFeAsO and NdFeAsO of 70–100 μm have been grown from alkali-metal chloride flux.[9,10] By applying pressure also SmFeAsO single crystals of up to 150 μm have been obtained.[11,12] Using high pressure and arsenic as flux, Ishikado *et al.* obtained large single crystals of PrFeAsO.[13] From pellets of NdFeAsO and LaFeAsO synthesized at high pressure, Martin *et al.* have been able to isolate crystals with a size up to half a millimeter.[14] Ambient pressure crystal-growth yielding large single crystals were done by Yan *et al.*[15] for LaFeAsO using NaAs and by Jesche *et al.*[16] for CeFeAsO using Sn as flux.

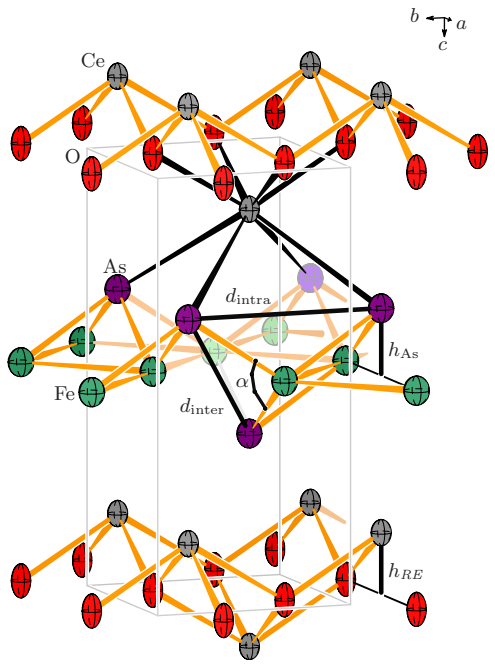

FIG. 1. (Color online) Crystal structure of CeFeAsO (space group $P4/nmm$, No. 129). The displacement ellipsoids represent 95% localization probability. The black bonds emphasize the square antiprismatic coordination of the rare-earth metal atom by four oxygen atoms and four arsenic atoms. h_{As} is the height of the arsenic atoms above the plane of iron atoms. h_R is the height of the rare-earth metal atom above the plane of oxygen atoms. d_{intra} is the shortest intraplane distance between two arsenic atoms and equals the lattice parameter a. d_{inter} is the interplane distance between two arsenic atoms above and below the iron atom net. The angle α is often referred to as the tetrahedral angle and indicates the deviation from a tetrahedral coordination of the iron atom.

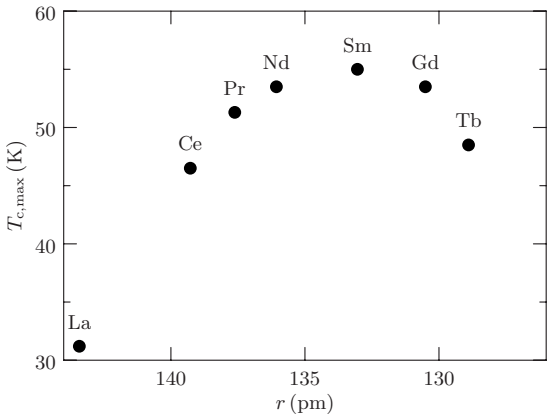

FIG. 2. Evolution of the maximum T_c for RFeAsO$_{1-\delta}$ (Refs. 5–7) over the effective rare-earth metal atom radii of RFeAsO.

However, no structural investigation has been conducted on a series of R-1111 obtained by the same single-crystal-growth technique.

Here, we present an ambient pressure method of single-crystal growth from flux for RFeAsO (R=La, Ce, Pr, Nd, Sm, Gd, and Tb). Atomic parameters were obtained by single-crystal x-ray diffraction and cell parameters were determined by LeBail fits of powder x-ray diffraction data against LaB_6 standard, yielding a consistent set of structural data. Moreover, anisotropic displacement parameters for the entire series of R-1111 are presented. In the light of these data, the influence of the rare-earth metal atom substitution and electron doping on the structural parameters is discussed.

II. EXPERIMENTAL

The starting materials were handled in an argon-filled glovebox [M. Braun, $p(O_2) \leq 1$ ppm, $p(H_2O) \leq 1$ ppm, argon purification with molecular sieve and copper catalyst]. Iron(II)-oxide powder (99.9%, Sigma-Aldrich Chemie GmbH, iron content checked by titration), arsenic (99.999% Alfa Aeser GmbH & Co. KG), and the corresponding freshly filed rare-earth metal (lanthanum, cerium, praseodymium, and neodymium: 99.9%, Treibacher Industie AG; samarium: 99.9%, Chempur GmbH; gadolinium: 99.9%, ABCR GmbH & Co. KG; and terbium: 99.9%, Acros Organics BVBA) were mixed and transferred into glassy carbon crucibles. 300–500 wt.-% of the eutectic mixture of NaI/KI (both 99.5%, Grüssing GmbH Analytika, dried at 650 K in dynamic vacuum) was stacked on top of the reactants as flux. Subsequently, the filled crucibles were sealed into silica ampoules under dynamic vacuum. To prevent high arsenic vapor pressures, the ampules were slowly heated to 1320 K within 24 h. An annealing period of three to six days was applied, followed by slow cooling to 870 K with 1 K/h. After quenching the ampules in air and removing the flux with de-ionized water, plate-shaped single crystals of the RFeAsO compounds suitable for structure and transport investigations were obtained.

First attempts to grow single crystals in accordance with previous studies on RTM_xAs_2 (TM=transition metal)[17] were conducted with rare-earth metal oxide (R_2O_3), arsenic, and iron as starting materials, and alkali-metal chlorides as flux. As observed before,[12] ROCl hindered the formation of phase-pure samples and single crystals of the target compounds. The less stable oxide iodides (ROI) are not formed when using sodium or potassium iodide. The exchange of rare-earth metal oxide by iron(III)-oxide or better by iron(II)-oxide as oxygen source improved single-crystal growth. However, the synthesis of RFeAsO with rare-earth metals heavier than terbium failed applying the NaI/KI flux method.

For single-crystal x-ray diffraction smaller crystals were chosen since larger crystals often showed broad reflection profiles due to stacking faults or mechanical stress as will be discussed later. The single crystals were isolated and cleaned in inert oil to keep the mechanical stress to a minimum. Subsequently, the crystals were sealed into glass capillaries only immobilized by adhesion to the glass wall by residual oil.

Single-crystal x-ray diffraction data were collected at 293(1) K on a Bruker SMART diffractometer using a molybdenum x-ray source and graphite monochromator (Mo $K\alpha$). Numerical absorption correction was applied using SADABS.[18] Structure solution and refinement were done with SHELXS and SHELXL,[19] respectively. Further details of the crystal structure investigations may be obtained from Fachinformationszentrum Karlsruhe, 76344 Eggenstein-Leopoldshafen, Germany [FAX: (+49)7247–808–666; crysdata@fiz-karlsruhe.de,http://www.fiz-karlsruhe.de/] on quoting the CSD numbers 421998 (R=La), 421999 (Ce), 422000 (Pr), 422001 (Nd), 422002 (Sm), 422003 (Gd), and 422004 (Tb).

ω scans of single reflections were done with APEX2[20] by rotating 1°. The crystals were cooled with a nitrogen gas stream using a Cryostream Controller 700 by Oxford Cryosystems for low-temperature ω scans.

Powder x-ray diffraction patterns were measured at 293(1) K on a Stadi P diffractometer (Stoe & Cie., Darmstadt, Cu $K\alpha_1$, Ge monochromator). Lattice constants were refined by a LeBail pattern decomposition against an internal LaB_6 standard using GSAS[21] and EXPGUI.[22] Pseudo-Voigt profile functions with a model for axial divergence were applied to fit the measured data.

Growth features, crystal composition, and flux incorporation were checked by scanning electron microscopy and energy dispersive x-ray (EDX) spectroscopy at an Ultra55 FEG-microscope (Carl Zeiss NTS GmbH) with a XFlash EDX-detector 4010 (Silicon Drift Detector) assembling a Quantax 400 (Bruker AXS Microanalysis GmbH). The EDX detector was calibrated with germanium standard.

Electrical resistivity measurements were carried out in a standard four-probe geometry in the temperature range of 1.8–300 K by using a commercial physical property measurement system (PPMS, Quantum Design).

III. RESULTS

Single crystals suitable for x-ray diffraction measurements were obtained for all RFeAsO (R=La, Ce, Pr, Nd, Sm,

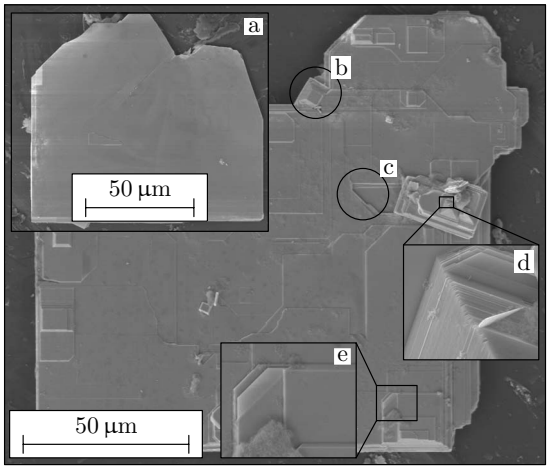

FIG. 3. (a) Scanning electron microscope (SEM) image of a NdFeAsO crystal used for single-crystal x-ray diffraction studies. (b)–(e) SEM image of a GdFeAsO crystal showing common growth instabilities of larger crystals: (b) additional crystal intergrown in random orientation; (c)–(e) free grown planes.

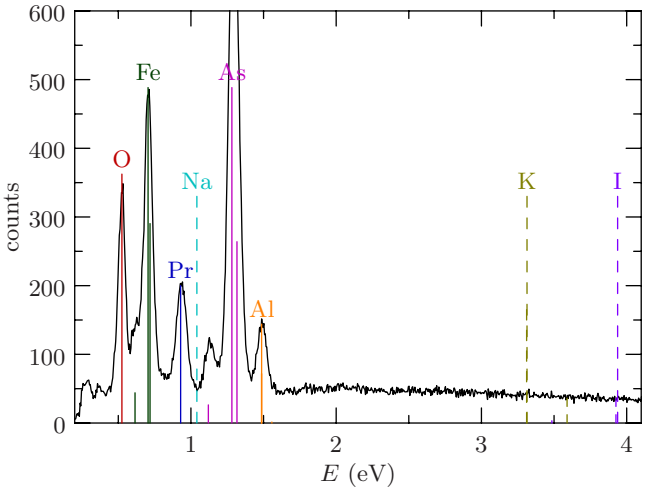

FIG. 4. (Color online) EDX spectrum of PrFeAsO. Characteristic lines of the elements of the flux (positions marked by dashed lines) are not observed. The aluminum signal originates from the specimen holder.

Gd, and Tb). Larger crystals were observed especially for the heavier rare-earth metals Gd and Tb. Whereas the size generally ranged from 30 to 300 μm for all R-1111, a crystal of half a millimeter size was obtained for TbFeAsO.

Figure 3 depicts the usual growth features of the single crystals. The crystal growth for RFeAsO is generally much faster in the ab plane than along the c axis. Accordingly, the platelets with a length of up to 300 μm are only few microns thick rendering the crystals very fragile. Mechanical stresses can easily lead to bending, splitting, or fracture of the crystal, which causes broad reflection profiles in single-crystal x-ray diffraction. Additionally, the larger crystals often show free growing planes [Figs. 3(c)–3(e)], which can cause flux incorporation. Furthermore, intergrowth of crystals in random orientation to the main crystal [Fig. 3(b)] was observed for larger crystals, hampering single-crystal x-ray diffraction investigations. Smaller single crystals [Fig. 3(a)] are of better quality, resulting in acceptable full width at half maximum of the Bragg reflections.

Within the accuracy of the EDX measurement the composition of the crystals was proved to be 1:1:1:1. Characteristic emission lines of neither potassium nor iodine were observed, thus substantial inclusion or incorporation of the flux material can be excluded. Yet the case of sodium is more complex since the emission lines are often covered by the signal of the rare-earth metals. However, in the case of PrFeAsO also sodium could definitively be excluded, as can be seen in Fig. 4.

The parameters of single-crystal x-ray diffraction data collections and the results of the crystal structure refinements of the quarternary iron pnictides are presented in Table I. The lattice parameters from powder diffraction and atomic data from single-crystal diffraction are compiled in Table II.

Using NaI/KI flux we obtained single crystals, which are not only sufficient for crystallographic investigations but also large enough to measure the electrical resistivity along the basal plane with a standard four-probe geometry (Fig. 5, inset). Over the entire temperature range the resistivity of TbFeAsO varies only between 0.85 and 1.05 mΩ cm. The room-temperature resistivity, $\rho_{300\ \mathrm{K}} \approx 1$ mΩ cm, indicates poor metallicity. Upon cooling the resistivity of TbFeAsO passes a minimum at about 180 K toward a local maximum centered at $T_S = 112$ K, marking the structural transition and the magnetic ordering of iron, which occurs at a slightly lower temperature than reported for polycrystalline material [$T = 122$ K (Ref. 24)]. Below $T = 75$ K, $\rho(T)$ increases again, showing similarities to LaFeAsO,[2] followed by a decrease at $T < 18$ K. The decrease of $\rho(T)$ changes slope toward lower temperature with a linear temperature dependence at $T < 6$ K. The onset of the anomaly at $T \approx 20$ K is also observable in polycrystalline material where no data are reported for $T \leq 19$ K.[24] A similar behavior was published for NdFeAsO, where the change of the magnetic structure of Fe at $T = 15$ K results in a significant decrease in the electrical resistivity of single-crystalline material with the current in the ab plane.[25] The TbFeAsO single crystal measured (Fig. 5) has a thickness of only 10 μm and is accordingly sensitive to strain caused by the wires and silver-paint contacts. Small deformation can result in cracks along the sample, which might be responsible for the observed differences to polycrystalline material. Applying a magnetic field of $\mu_0 H = 1$ T has no significant influence on the structural transition at T_S and leads to a small negative magnetoresistance at lower temperatures. The decrease in the electrical resistivity occurring at $T = 18$ K in zero field is shifted to $T = 14$ K.

Splitting of the tetragonal Bragg reflection 800 occurring below 160 K is demonstrated exemplarily for LaFeAsO (Fig. 6), indicating the structural transition from space group $P4/nmm$ to $Cmme$ as expected for undoped LaFeAsO.[26]

IV. DISCUSSION

To assess the influence of the rare-earth metal substitution on the structure of R-1111 and thereby on superconductivity,

TABLE I. Parameters of single-crystal x-ray diffraction data collection at 293(1) K and results of the structural refinement of *R*FeAsO.

R	θ_{max} (deg)	R_{int}	R_σ	R_1	wR_2	*S*	$\Delta\rho_{max,min}$ (e^- Å^{-3})
La	37.52	0.037	0.016	0.027	0.023	2.22	1.69,–1.59
Ce	37.57	0.034	0.016	0.024	0.025	2.28	1.52,–1.87
Pr	37.65	0.039	0.017	0.025	0.018	1.66	2.01,–2.70
Nd	39.78	0.017	0.009	0.018	0.018	3.11	1.74,–1.15
Sm	37.57	0.024	0.010	0.011	0.013	1.92	0.89,–1.41
Gd	37.66	0.025	0.016	0.024	0.025	2.58	2.23,–2.25
Tb	37.52	0.018	0.009	0.012	0.016	2.51	1.20,–1.04

a suitable scale has to be defined. Often, the radii of the substituted atoms are used since a linear correlation to the volume of the structure is expected in analogy to Vegard's law.

As depicted in Fig. 1, the rare-earth metal atom is coordinated by four oxygen atoms and four arsenic atoms. This suggests the use of the radii for eightfold coordinated R^{3+} ions as revised by Shannon[23] and originally deduced by Greis and Petzel[27] from the ninefold coordination in RF_3 where the coordination polyhedron is assembled by equal anions at almost equal distances.

However, in *R*FeAsO the square spanned by the four arsenic atoms is twice as large as the square spanned by the oxygen atoms, leading to a strong distortion of the square antiprism with a large difference in cation-anion distances ($\bar{d}_{R\text{-O}} \approx 230$ pm, $\bar{d}_{R\text{-As}} \approx 330$ pm). The more inhomogeneous coordination in *R*FeAsO compared to the coordination in RF_3 creates a deviation from linearity of the volume evolution over the chosen rare-earth metal radii in eightfold coordination as shown in Fig. 7.

Thorough investigation of the crystal structures of *R*-1111 reveals that the interplane distance of the arsenic atoms (Fig. 1) is constant(!), $\bar{d}_{inter}=389.4(4)$ pm. It appears to be the minimum distance arsenic atoms can attain in undoped *R*FeAsO (*R*=La, Ce, Pr, Nd, Sm, Gd, and Tb). The intraplane distance of the arsenic atoms, d_{intra} (Fig. 1), is equal to the *a* axis and longer than d_{inter}. Going from lanthanum to terbium as depicted in Fig. 8, the intraplane distance approaches the interplane distance of the arsenic atoms preventing a further shrinkage of the structure. Consequently, all *R*FeAsO compounds with smaller rare-earth metal atoms (*R*=Dy,Ho,…) have to be synthesized under external pressure as described in the literature.[9,28,29]

The iron-arsenic layer in TbFeAsO can thus be considered as a section of a body-centered-cubic packing of arsenic atoms with iron atoms situated in the tetrahedral voids.

With d_{inter} being constant over the rare-earth substitution and the interaction between *R*, As, and O being predominantly ionic, as argued by Blanchard *et al.*,[30] the structure of *R*FeAsO can be analyzed in a hard-sphere model (Fig. 8). The radius of the arsenic sphere is $r_{As}=\frac{1}{2}d_{inter}$. The radius of the iron sphere is deduced from the shortest interatomic distance of iron and arsenic atoms, $r_{Fe}=d_{As\text{-}Fe}-r_{As}$. The same can be done for the radius of the rare-earth metal sphere ($r_R=d_{As\text{-}R}-r_{As}$). The radius of the oxygen sphere cannot be determined directly from d_{inter} and has to be calculated from the radius of the rare-earth metal sphere and the shortest interatomic distance of oxygen and rare-earth metal atom ($r_O=d_{R\text{-}O}-r_R$).

TABLE II. Structural parameters of *R*FeAsO in space group $P4/nmm$ (No. 129) and $Z=2$ measured at 293(1) K. Cell parameters were determined by the LeBail fits of powder x-ray diffraction patterns. Atomic positions and anisotropic displacement parameters were refined from single-crystal x-ray diffraction data.

				R [a]			As			Fe		O	
R	*r* (pm)[b]	*a* (pm)	*c* (pm)	*z*	U_{11} [c]	U_{33}	*z*	U_{11}	U_{33}	U_{11}	U_{33}	U_{11}	U_{33}
La	130	403.67(1)	872.18(4)	0.14141(5)	57(1)	85(2)	0.65138(9)	85(2)	107(4)	88(3)	106(5)	68(14)	142(27)
Ce	128.3	400.58(1)	862.89(6)	0.14106(4)	50(1)	85(2)	0.65442(8)	79(2)	102(3)	81(3)	105(5)	46(12)	145(24)
Pr	126.6	398.89(1)	859.66(8)	0.13960(4)	62(1)	96(2)	0.65608(7)	86(2)	107(3)	87(2)	121(4)	74(11)	94(20)
Nd	124.9	397.13(1)	856.55(5)	0.13899(3)	61(1)	93(1)	0.65725(6)	85(2)	107(3)	84(2)	109(4)	69(10)	120(18)
Sm	121.9	394.69(2)	849.65(6)	0.13705(2)	56(1)	88(1)	0.66007(4)	80(1)	96(2)	78(2)	108(3)	65(8)	77(12)
Gd	119.3	391.99(3)	844.51(8)	0.13570(5)	69(1)	98(2)	0.6623(1)	92(2)	109(5)	93(4)	112(7)	24(14)	97(32)
Tb	118	390.43(3)	840.8(1)	0.13455(3)	57(1)	69(1)	0.66389(6)	80(1)	76(3)	76(2)	100(4)	59(8)	115(19)

[a] *R*, As: 2*c*, $x=1/4$, $y=1/4$, *z*; Fe: 2*b*, $x=3/4$, $y=1/4$, $z=1/2$; and O: 2*a*, $x=3/4$, $y=1/4$, $z=0$.
[b] Radii of the corresponding trivalent rare-earth metal in octahedral coordination from Ref. 23.
[c] All U_{ij} in pm^2, $U_{11}=U_{22}$, $U_{12}=U_{23}=U_{13}=0$.

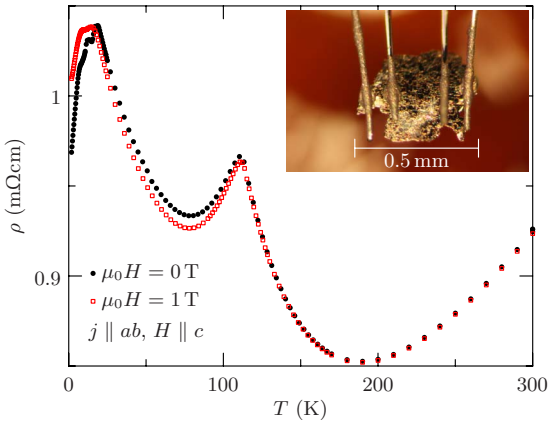

FIG. 5. (Color online) Temperature dependence of the electrical resistivity of a TbFeAsO single crystal (shown in the inset) in the *ab* plane. The local maximum at T_S=112 K results from a structural transition.

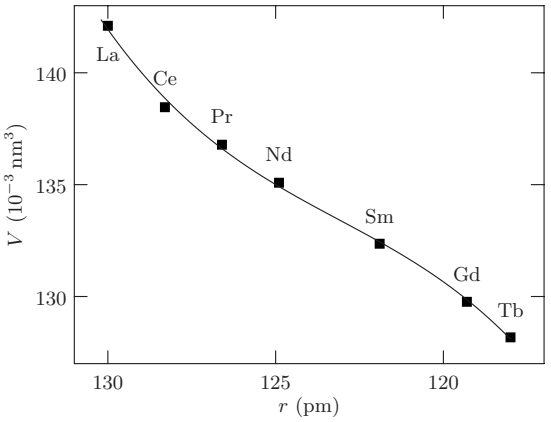

FIG. 7. Unit cell volume of *R*FeAsO over the rare-earth metal radii as compiled by Shannon (Ref. 23) for eightfold coordinated trivalent ions. The error bars are within the size of the symbols.

The resulting effective radii are listed in Table III. According to the hard-sphere model, all radii except those of the rare-earth metal atoms should be almost constant. Indeed, the deviations in the calculated values are small, yet exhibit the limits of the model, which does not account for polarization effects or covalent bonding. Nevertheless, the changes of the rare-earth metal atom radii (r_R) are one order of magnitude larger than those of the other atoms. The above-mentioned geometrical limit of the *R*FeAsO series with *R* =Tb can clearly be seen by the equalization of $d_{\text{intra}} \equiv a$ and $d_{\text{inter}} \equiv 2r_{\text{As}}$.

Additionally, the sphere packing can be checked by the anisotropy of vibration,

$$f = \frac{U_{33} - U_{11}}{(2U_{11} + U_{33})/3},$$

which indicates the elongation of the displacement ellipsoid along the *c* axis, with f=0 referring to an isotropic vibration. For all *R* the arsenic atom shows almost the same anisotropy of vibration (Fig. 9). Only for the densely packed situation of TbFeAsO isotropic displacement is observed. For the vibration of the heavier rare-earth atoms the trend toward diminished anisotropy is observed, too.

Using the effective radii of *R* as a scale to compare the influence of the rare-earth metal substitution on the structure of *R*-1111 leads to a linear evolution of structural features such as the volume or the height of the arsenic atom over the square iron net (Fig. 10). Although LaFeAsO fits the linear evolution of the volume of *R*FeAsO, it deviates slightly from the linear trends in the height of the arsenic atom over the square iron net (h_{As}=[z_{As}−0.5]*c*) and in the height of the rare-earth metal atom over the oxygen layer (h_R=z_R*c*). Since the radius for the rare-earth metal atom is deduced from the interatomic distance of arsenic and the rare-earth metal, closer coordination toward oxygen than expected from linear extrapolation results in a comparatively large effective radius for the f^0-cation La^{3+} (Table III). This is consistent with the larger decrease in $T_{c,\text{max}}$ from $CeFeAsO_{1-\delta}$ (46.5 K) to $LaFeAsO_{1-\delta}$ (31.2 K) compared to the decrease from $PrFeAsO_{1-\delta}$ (51.3 K) (Ref. 5) to $CeFeAsO_{1-\delta}$, as can be seen in Fig. 2.

The exceptional position of LaFeAsO can also be observed in the normalized interatomic distances *D* as depicted in Fig. 11. The largest changes in interatomic distances are observed for the interactions directly influenced by the rare-

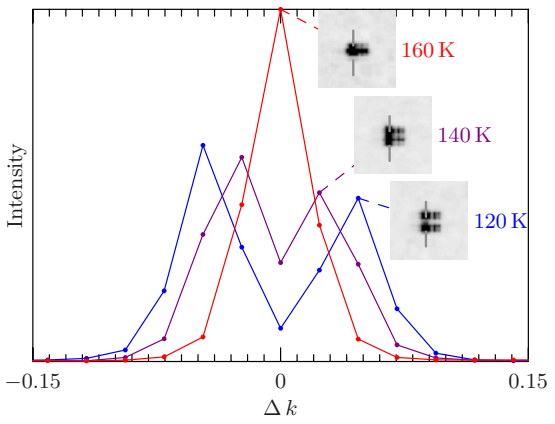

FIG. 6. (Color online) ω scan of the Mo $K\alpha_1$ and $K\alpha_2$ Bragg reflections 800 of LaFeAsO showing a splitting on cooling below the tetragonal to orthorhombic transition. Lines are guides for the eyes. The data points correspond to the resolution of the area detector.

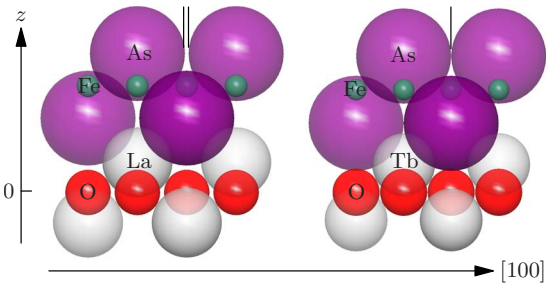

FIG. 8. (Color online) Hard-sphere model representation of LaFeAsO (left) and TbFeAsO (right). The intraplane distance (see Fig. 1) of the arsenic atoms approaches the interplane distance going from lanthanum to terbium.

TABLE III. Calculated effective radii of the atoms in *R*FeAsO as deduced from the hard-sphere model. The errors are estimated by combined variances.

R	r_R (pm)	r_{Fe} (pm)	r_{As} [a] (pm)	$\frac{1}{2}a$ [b] (pm)	r_O (pm)
La	143.42(9)	46.76(7)	194.42(6)	201.84(1)	93.12(9)
Ce	139.28(8)	46.11(7)	194.46(5)	200.29(1)	95.10(8)
Pr	137.62(8)	45.72(6)	194.66(5)	199.45(1)	95.15(8)
Nd	136.06(6)	45.37(5)	194.57(4)	198.57(1)	95.45(6)
Sm	133.17(5)	44.81(4)	194.86(3)	197.35(1)	95.97(5)
Gd	130.5(1)	44.2(1)	194.94(7)	196.00(2)	96.5(1)
Tb	128.90(7)	43.90(6)	195.05(5)	195.22(2)	96.73(8)

[a] $r_{As}=\frac{1}{2}d_{inter}$.
[b] $\frac{1}{2}a=\frac{1}{2}d_{intra}$.

earth metal substitution: $d_{R\text{-As}}$, $d_{R\text{-O}}$, and d_{intra} decrease monotonically, with the latter corresponding to the a parameter. The interatomic distances between iron and arsenic (not shown in the figure) and the interplane distance of the arsenic atoms are almost invariant to rare-earth metal substitution.

To assess the influence of oxygen vacancy concentration on the structure of *R*FeAsO, literature data for $NdFeAsO_{1-\delta}$ from Lee *et al.*[31] were also evaluated with the hard-sphere model (open symbols in Figs. 10 and 11). Oxygen deficiency weakens the bonding in the NdO layer. The distance between oxygen and neodymium atoms as well as h^{δ}_{Nd} increases slightly. The weakened Nd-O bonding and the higher charge of the $(NdO_{1-\delta})^{(1+2\delta)+}$ and $(FeAs)^{(1+2\delta)-}$ layers is compensated by stronger Nd-As bonding. The shorter $d^{\delta}_{Nd\text{-}As}$ results in smaller r_{Nd}. Concurrently, the distance of arsenic atoms to the iron layer h^{δ}_{As} is enlarged. As the interplane As-As distance increases, the geometrical limit of the structure type is changed. Further contraction (here due to cooling from RT to 10 K) leads again to the equalization of d_{inter} and d_{intra}, however, at a value that is about 4 pm larger.

As depicted by Lee *et al.*,[31] the angle α of the doped *R*FeAsO compounds at low temperatures is a reasonable indicator for $T_{c,max}$, which is highest for the tetrahedral angle of 109.5°. However, the structural arguments do not suffice. Taking $LaFeAsO_{1-x}F_x$ as an example, doping triggers superconductivity at $x\approx0.05$, with $T_{c,max}\approx24$ K at $x\approx0.1$, and a subsequent suppression of superconductivity at higher doping levels.[32] Geometrically, the increase in doping should further increase α toward the ideal tetrahedral coordination for the iron atoms, with a further increase in T_c. It can thus be argued that high-T_c values originate from a coincidence of electronical and structural optima.

Comparing the influence of rare-earth substitution exemplarily with the data of oxygen deficiency doping data of Lee *et al.* shows the high impact of electronical doping on the structure. Kuroki *et al.*[8] indicated the strong influence of h_{As} on the electronical structure of *R*-1111. It was predicted that the combination of large cell volume V and increased height of the arsenic atom h_{As} results in high-T_c. As can be deduced from the diametric trends in Fig. 10, a medium sized rare-earth metal atom in combination with a large

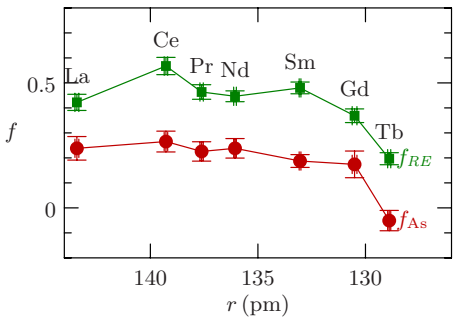

FIG. 9. (Color online) Anisotropy of vibration f of the arsenic and rare-earth atoms in *R*FeAsO with $f=0$ indicating an isotropic vibrational behavior. Connecting lines are guides for the eyes. Error bars by combined variances.

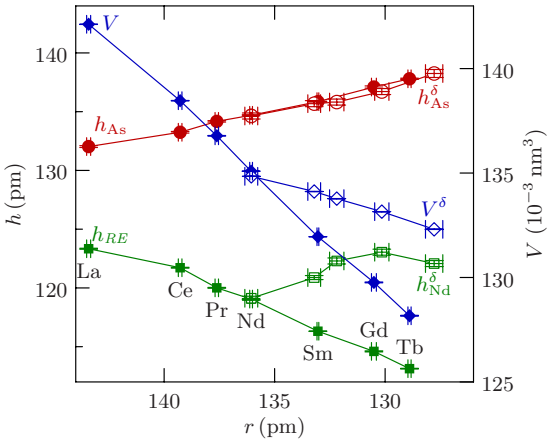

FIG. 10. (Color online) The height of the arsenic atom (h_{As}, see Fig. 1) over the iron plane, the height of the rare-earth metal atom (h_R, see Fig. 1) over the oxygen layer, and the volume V over the effective radii of the trivalent rare-earth metal deduced form the hard-sphere model. The open symbols represent data for $NdFeAsO_{1-\delta}$ (Ref. 31). From left to right: $\delta=0.05(1)$, RT, non-superconducting; $\delta=0.080(9)$, RT, $T_c=35$ K; $\delta=0.14(1)$, RT, $T_c=44$ K; $\delta=0.17(1)$, RT, $T_c=51$ K; and $\delta=0.17(1)$, 10 K, $T_c=51$ K. Connecting lines are guides for the eyes. Error bars by combined variances.

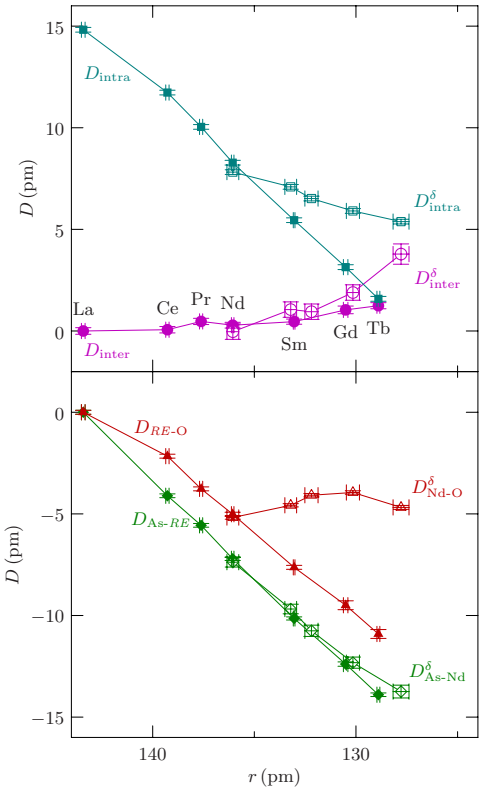

FIG. 11. (Color online) Plot of the normalized interatomic distances $D_{A\text{-}B}=d^{R\mathrm{FeAsO}}_{A\text{-}B}-d^{\mathrm{LaFeAsO}}_{A\text{-}B}$ with respect to LaFeAsO over the calculated effective rare-earth atom radii deduced form the hard-sphere model. For better comparison of the normalized intraplane and interplane distances of the arsenic atoms, D_{intra} is calculated by $d^{R\mathrm{FeAsO}}_{\mathrm{intra}}-d^{\mathrm{LaFeAsO}}_{\mathrm{inter}}$. The open symbols represent data for $NdFeAsO_{1-\delta}$ (Ref. 31). From left to right: δ=0.05(1), RT, nonsuperconducting; δ=0.080(9), RT, T_c=35 K; δ=0.14(1), RT, T_c=44 K; δ=0.17(1), RT, T_c=51 K; and δ=0.17(1), 10 K, T_c=51 K. Connecting lines are guides for the eyes. Error bars by combined variances.

oxygen deficiency should be used. In accordance with experimental data, $NdFeAsO_{1-\delta}$ seems to be close to the optimum.

V. CONCLUSIONS

Using alkali-metal iodides as flux facilitated the free growth of *R*FeAsO (*R*=La, Ce, Pr, Nd, Sm, Gd, and Tb) single crystals suitable for resistivity measurements and single-crystal x-ray diffraction studies. The elaborated consistent set of structural data for the *R*-1111 compounds and the comparison with structural data of $NdFeAsO_{1-\delta}$ from literature allowed a thorough investigation of the influence of the rare-earth metal substitution and doping on the structural features of *R*-1111.

A hard-sphere model proved to be suitable for the interpretation of structural trends. The thereby revealed geometrical limit for the structure type rationalizes the failure of ambient pressure synthesis of heavier *R*-1111 then TbFeAsO.

Additionally, an interplay of electronical and structural optima for high-T_c values is proposed.

The structural data also provide a reliable basis for theoretical investigations of the electronic structure of the undoped compounds and their relation to their superconducting congeners.

Further single-crystal studies of doped *R*FeAsO compounds and the evolution over the temperature will help to complete the geometrical model of the iron-based superconductors.

ACKNOWLEDGMENT

The authors like to thank Jutta Krug, Alexander Gerisch, and Tilmann Meusel for their help with sample preparation and measurements.

[1] Y. Kamihara, H. Hiramatsu, M. Hirano, R. Kawamura, H. Yanagi, T. Kamiya, and H. Hosono, J. Am. Chem. Soc. **128**, 10012 (2006).
[2] Y. Kamihara, T. Watanabe, M. Hirano, and H. Hosono, J. Am. Chem. Soc. **130**, 3296 (2008).
[3] H.-H. Wen, G. Mu, L. Fang, H. Yang, and X. Zhu, EPL **82**, 17009 (2008).
[4] H. Takahashi, H. Okada, K. Igawa, Y. Kamihara, M. Hirano, and H. Hosono, Physica C **469**, 413 (2009).
[5] Z.-A. Ren, G.-C. Che, X.-L. Dong, J. Yang, W. Lu, W. Yi, X.-L. Shen, Z.-C. Li, L.-L. Sun, F. Zhou, and Z.-X. Zhao, EPL **83**, 17002 (2008).
[6] J. Yang, Z.-C. Li, W. Lu, W. Yi, X.-L. Shen, Z.-A. Ren, G.-C. Che, X.-L. Dong, L.-L. Sun, F. Zhou, and Z.-X. Zhao, Supercond. Sci. Technol. **21**, 082001 (2008).
[7] J. Yang, X.-L. Shen, W. Lu, W. Yi, Z. C. Li, Z.-A. Ren, G.-C. Che, X.-L. Dong, L.-L. Sun, F. Zhou, and Z.-X. Zhao, New J. Phys. **11**, 025005 (2009).
[8] K. Kuroki, H. Usui, S. Onari, R. Arita, and H. Aoki, Phys. Rev. B **79**, 224511 (2009).
[9] P. Quebe, L. J. Terbuchte, and W. Jeitschko, J. Alloys Compd. **302**, 70 (2000).
[10] L. Fang, P. Cheng, Y. Jia, X. Zhu, H. Luo, G. Mu, C. Gu, and H.-H. Wen, J. Cryst. Growth **311**, 358 (2009).
[11] N. D. Zhigadlo, S. Katrych, Z. Bukowski, S. Weyeneth, R. Puzniak, and J. Karpinski, J. Phys.: Condens. Matter **20**, 342202 (2008).
[12] J. Karpinski, N. D. Zhigadlo, S. Katrych, Z. Bukowski, P. Moll, S. Weyeneth, H. Keller, R. Puzniak, M. Tortello, D. Daghero, R. Gonnelli, I. Maggio-Aprile, Y. Fasano, O. Fischer, K. Rogacki, and B. Batlogg, Physica C **469**, 370 (2009).
[13] M. Ishikado, S. Shamoto, H. Kito, A. Iyo, H. Eisaki, T. Ito, and Y. Tomioka, Physica C **469**, 901 (2009).
[14] C. Martin, M. E. Tillman, H. Kim, M. A. Tanatar, S. K. Kim, A. Kreyssig, R. T. Gordon, M. D. Vannette, S. Nandi, V. G. Kogan, S. L. Bud'ko, P. C. Canfield, A. I. Goldman, and R. Prozorov,

Phys. Rev. Lett. **102**, 247002 (2009).
[15] J.-Q. Yan, S. Nandi, J. L. Zarestky, W. Tian, A. Kreyssig, B. Jensen, A. Kracher, K. W. Dennis, R. J. McQueeney, A. I. Goldman, R. W. McCallum, and T. A. Lograsso, Appl. Phys. Lett. **95**, 222504 (2009).
[16] A. Jesche, C. Krellner, M. de Souza, M. Lang, and C. Geibel, New J. Phys. **11**, 103050 (2009).
[17] D. Rutzinger, C. Bartsch, M. Doerr, H. Rosner, V. Neu, T. Doert, and M. Ruck, J. Solid State Chem. **183**, 510 (2010).
[18] G. M. Sheldrick, SADABS (Version 2008/1), Bruker AXS, Inc., 2008.
[19] G. M. Sheldrick, Acta Crystallogr., Sect. A: Found. Crystallogr. **64**, 112 (2008).
[20] APEX2 (Version 2009.9), Bruker AXS, Inc., 2009.
[21] A. C. Larson and R. B. V. Dreele, LAUR Report No. 86-748, 2000 (unpublished).
[22] B. H. Toby, J. Appl. Crystallogr. **34**, 210 (2001).
[23] R. D. Shannon, Acta Crystallogr., Sect. A: Cryst. Phys., Diffr., Theor. Gen. Crystallogr. **32**, 751 (1976).
[24] Y. Luo, Q. Tao, Y. Li, X. Lin, L. Li, G. Cao, Z.-A. Xu, Y. Xue, H. Kaneko, A. V. Savinkov, H. Suzuki, C. Fang, and J. Hu, Phys. Rev. B **80**, 224511 (2009).
[25] W. Tian, W. Ratcliff, II, M. Kim, J. Yan, P. Kienzle, Q. Huang, B. Jensen, K. Dennis, R. McCallum, T. Lograsso, R. McQueeney, A. Goldman, J. Lynn, and A. Kreyssig, Phys. Rev. B **82**, 060514(R) (2010).
[26] C. de la Cruz, Q. Huang, J. W. Lynn, J. Li, W. Ratcliff, II, J. L. Zarestky, H. A. Mook, G. F. Chen, J. L. Luo, N. L. Wang, and P. Dai, Nature (London) **453**, 899 (2008).
[27] O. Greis and T. Petzel, Z. Anorg. Allg. Chem. **403**, 1 (1974).
[28] J.-W. G. Bos, G. B. S. Penny, J. A. Rodgers, D. A. Sokolov, A. D. Huxley, and J. P. Attfield, Chem. Commun. (Cambridge) (2008), 3634.
[29] J. A. Rodgers, G. B. S. Penny, A. Marcinkova, Jan-Willem G. Bos, D. A. Sokolov, A. Kusmartseva, A. D. Huxley, and J. P. Attfield, Phys. Rev. B **80**, 052508 (2009).
[30] P. E. R. Blanchard, R. G. Cavell, and A. Mar, J. Solid State Chem. **183**, 1477 (2010).
[31] C. H. Lee, A. Iyo, H. Eisaki, H. Kito, M. T. Fernandez-Diaz, T. Ito, K. Kihou, H. Matsuhata, M. Braden, and K. Yamada, J. Phys. Soc. Jpn. **77**, 083704 (2008).
[32] H. Luetkens, H.-H. Klauss, M. Kraken, F. J. Litterst, T. Dellmann, R. Klingeler, C. Hess, R. Khasanov, A. Amato, C. Baines, M. Kosmala, O. J. Schumann, M. Braden, J. Hamann-Borrero, N. Leps, A. Kondrat, G. Behr, J. Werner, and B. Buchner, Nature Mater. **8**, 305 (2009).